Separation measurement of two freely rotating dipole emitters at near optimal precision

SHENG LIU,[1] SUJEET PANI,[1,2] SAJJAD A. KHAN,[1,3] FRANCISCO E. BECERRA,[1,2] AND KEITH A. LIDKE [1,*]

[1] *Department of Physics and Astronomy, University of New Mexico, Albuquerque, New Mexico, USA*
[2] *Center for Quantum Information and Control, University of New Mexico, Albuquerque, New Mexico, USA*
[3] *Nanoscience and Microsystems Engineering, University of New Mexico, Albuquerque, New Mexico, USA*
[*] *klidke@unm.edu*

Abstract: According to Rayleigh's criterion, two incoherent emitters with a separation below the diffraction limit are not resolvable with a conventional fluorescence microscope. One method of Super-Resolution Microscopy (SRM) breaks the diffraction-limited resolution by precisely estimating the centroid position of spatiotemporally independent emitters. However, conventional detection methods of SRM techniques are not optimal for estimating the separation of two simultaneously excited emitters. Recently, a number of detection methods based on modal imaging were developed to achieve the quantum Cramér-Rao lower bound (QCRB) for estimating separations between two nearby emitters. The QCRB determines the minimum achievable precision across all possible detection methods. Current modal imaging techniques assume a scalar field generated from a point source, such as an optical fiber or a pinhole. However, for fluorescently labeled samples, point emitters are single fluorophores that can be modeled as dipole emitters, and in practice are often freely rotating. Dipole radiation must be expressed in vectorial theory and the assumption of a scalar field no longer holds. Here we propose a detection scheme based on one of the modal imaging techniques, super-localization by image inversion interferometry (SLIVER), for separation estimation of two freely rotating dipoles. We introduce a vortex wave plate before the SLIVER detection to separate the radial and azimuthal components of the dipole radiation. We demonstrated that our method achieves near constant precision independent of the separation between two dipole emitters. We also quantified the effect of numerical aperture, detection bandwidth, number of estimation parameters, background and misalignment on separation estimation. Our method provides a near optimal detection scheme for measuring the separation of two freely-rotating dipole emitters such as fluorescently tagged molecules.

1. Introduction

Rayleigh's criterion is commonly used to assess the resolution of an imaging system and provides a definition of the minimum separation where two emitters are resolvable [1]. This resolution limit is termed as diffraction limited resolution and can be approximated to the width of the impulse response of a imaging system, the point spread function (PSF) [2]. Given the output response and the PSF model for a particular imaging system, the estimation precisions of unknown parameters are bounded by classical Cramér-Rao lower Bound (CRB) [3, 4]. CRB is widely used in single molecule localization microscopy (SMLM) to determine the localization precision of a point emitter [5–11]. The detection methods for most SMLM systems can be categorized as direct detection, where the electric field from a point source was directed to the detector without any spatial variant modification. In other words, the input field of direct detection is projected to a constant spatial mode or multiplied by a scalar. For direct detection of two emitters, the CRB of separation estimation diverges quickly towards infinity as the separation decreases much below the diffraction limited resolution [12, 13]. The CRB depends on the particular measurement of an unknown parameter.

Quantum information theory provides a bound for any possible measurement allowed by

quantum mechanics, the Quantum CRB (QCRB) [12, 14–17]. This bound is not related to any particular measurement strategy. Finding a measurement strategy that can saturate this bound is a fundamental goal in quantum metrology [18, 19]. Tsang et al. derived the QCRB for estimating the separation of two scalar point sources and found that it is independent of their separation for a Gaussian PSF model. Significantly, they also proposed a measurement technique that achieves the QCRB [12, 20, 21]. This measurement technique is based on modal imaging, which decomposes the electric field into a set of orthogonal spatial modes, e.g. Hermite Gaussian modes, followed by signal detection of each spatial mode. Counting of the photon numbers in each mode can be used in an estimator that achieves the QCRB. A number of experimental realizations of modal imaging have been demonstrated. A straight forward implementation uses a spatial mode demultiplexing (SPADE) device (or a mode sorter), based on multi-plane interference imaging, to decompose the input field to orthogonal spatial modes [22, 23]. Alternatively, the input field can be sequentially projected to orthogonal modes by varying the modes of a local oscillator in a heterodyne detection [24–26] or by varying the amplitude modulation of a spatial light modulator [27]. On the other hand, some implementations project the input field onto fewer number of optical modes. For instance, super-resolved position localization by inversion of coherence along an edge (SPLICE) projects the input field onto a single spatial mode, which is generated by introducing a π phase shift between the top and bottom halves of the input field [28]. Alternatively, by inverting the input field in one of the arms of a Mach-Zehnder interferometer, super-localization by image inversion interferometry (SLIVER) decompose the input field into its symmetric and antisymmetric components. SLIVER was first proposed by Nair et al. [29], and later experimentally demonstrated by Tang et al. [30].

However, all previous implementations of modal imaging were demonstrated by generating the point source from a laser coupled into a single mode fiber and using a Gaussian PSF or PSFs that can be described by scalar diffraction theory, e.g. Airy pattern or sinc function [2]. In fluorescence imaging, point source is a single fluorophore, which is often modeled as a dipole emitter [11, 31–39]. The PSF of a static dipole emitter is described by vectorial diffraction theory and the PSF pattern varies with the dipole orientation. In many fluorescent labeled samples, the fluorophore can freely rotate in an aqueous medium and can be modeled as a freely rotating dipole, where the dipole rotation is much faster than the fluorescent lifetime so that the resulting radiation samples over all possible dipole orientations [33]. However, even with sampling from a freely rotating dipole, the PSF can not be simply approximated to a Gaussian: each emitted photon must be considered as originating from a static dipole and the response of the optical system treated with vectorial theory.

Here we investigated the effect of dipole radiation on measuring the separation of two point sources and proposed a near-optimal measurement scheme to estimate the separation of two freely rotating dipoles. In the proposed method, we introduce a vortex wave plate (VWP) to separate the radial and azimuthal components of the dipole radiation. The radial component is detected by direct detection for centroid estimation, and the azimuthal component is sent to SLIVER detection for separation estimation. We term this measurement as SLIVER(A)+DD(R). A similar configuration was previously proposed for optimal measurement of dipole orientation, but with the radial component entering the SLIVER detection [17].

In this study, we numerically investigated the separation estimation of two freely rotating dipoles using different detection methods. We quantified the effects of numerical aperture, detection bandwidth, the number of estimation parameters, background and misalignment on separation estimation. Our results demonstrate that the proposed detection scheme, SLIVER(A)+DD(R), outperforms other methods, especially at high numerical aperture. Under the ideal condition (perfect VWP, zero background and no misalignment), SLIVER(A)+DD(R) achieves near-constant precision on separation estimation, regardless of emitter's separations.

2. Theory

2.1. Detection methods

We consider five detection methods based on a combination of direct and SLIVER detections (Fig.1(a)) for measuring the separation of two freely rotating dipoles. The first is the conventional detection method for most fluorescence microscopes, termed direct detection (DD). The second method uses SLIVER detection, which consists of a Mach-Zehnder interferometer with one of its arm inverting the electric field in xy (Fig.1(e)). SLIVER detection decomposes the even and odd components of the input field into symmetric and antisymmetric channels. For example, if the input field $h(x, y)$ is even, $h(x, y) = h(-x, -y)$, the expected photon from the antisymmetric channel will be zero due to total destructive interference; if the input field is odd, $h(x, y) = -h(-x, -y)$, the expected photon from the symmetric channel will be zero. SLIVER requires the centroid of the two emitters to be aligned with the inversion center. However, SLIVER by itself cannot accurately measure the centroid position due to ambiguity and strong correlation between the centroid and separation estimation. To solve this problem, we use a hybrid method similar to the one proposed previously [12] and term it SLIVER+DD. In this method, the input field is split equally into two paths: one path is directed to SLIVER, while the other path is directed to DD. This measurement method provides three output channels, one from DD and two from SLIVER, where the output from DD is used for estimating the centroid of the two emitters. The fourth method, termed DD(A)+DD(R), decouples the radial and azimuthal components of the input field by adding a VWP after the objective. A perfect VWP converts the radially/azimuthally polarized beam ($\boldsymbol{E}_{\mathrm{R}}/\boldsymbol{E}_{\mathrm{A}}$) to horizontally/vertically ($\boldsymbol{E}_{\mathrm{H}}/\boldsymbol{E}_{\mathrm{V}}$) polarized beam with 100% efficiency. With a polarized beam splitter (PBS), the radial and azimuthal components of the dipole radiation can be separated. Each component is collected by a DD measurement. The last method, termed SLIVER(A)+DD(R), is our proposed method for measuring the separation of two freely rotating dipoles. In this configuration, the azimuthal component is collected by SLIVER while the radial component is collected by DD. This design is based on the fact that the azimuthal field of dipole radiation is purely odd, independent of dipole orientation (Fig.1(c)). Therefore, the symmetric channel from SLIVER will always have total destructive interference at any dipole orientation (Fig.1(a)). To quantify the degree of interference, we define visibility,

$$Vis = \frac{I_{\max} - I_{\min}}{I_{\max} + I_{\min}}. \tag{1}$$

For SLIVER detection, $I_{\max}$ and $I_{\min}$ represent the maximum and minimum total photons from the two output channels when imaging a single emitter located at the inversion center. The visibility achieved by SLIVER(A) is one for detecting a freely rotating dipole, ensuring non-zero Fisher information of separation estimation at any separation of two freely rotating dipoles (Supplement 1).

2.2. PSF calculation

The PSFs of those five detection methods can be calculated as follows,

$$I_{\mathrm{DD}} = I_{\mathrm{H}} + I_{\mathrm{V}}, \tag{2}$$

$$I_{\mathrm{SLIVER}} = \left[\frac{1}{2}\left(I_{\mathrm{sym,H}} + I_{\mathrm{sym,V}}\right), \frac{1}{2}\left(I_{\mathrm{asym,H}} + I_{\mathrm{asym,V}}\right)\right], \tag{3}$$

$$I_{\mathrm{SLIVER+DD}} = \left[\frac{1}{2}\left(I_{\mathrm{H}} + I_{\mathrm{V}}\right), \frac{1}{4}\left(I_{\mathrm{sym,H}} + I_{\mathrm{sym,V}}\right), \frac{1}{4}\left(I_{\mathrm{asym,H}} + I_{\mathrm{asym,V}}\right)\right], \tag{4}$$

$$I_{\mathrm{DD(A)+DD(R)}} = \left[I_{\mathrm{R}}, I_{\mathrm{A}}\right], \tag{5}$$

$$I_{\mathrm{SLIVER(A)+DD(R)}} = \left[I_{\mathrm{R}}, \frac{1}{2}I_{\mathrm{sym,A}}, \frac{1}{2}I_{\mathrm{asym,A}}\right]. \tag{6}$$

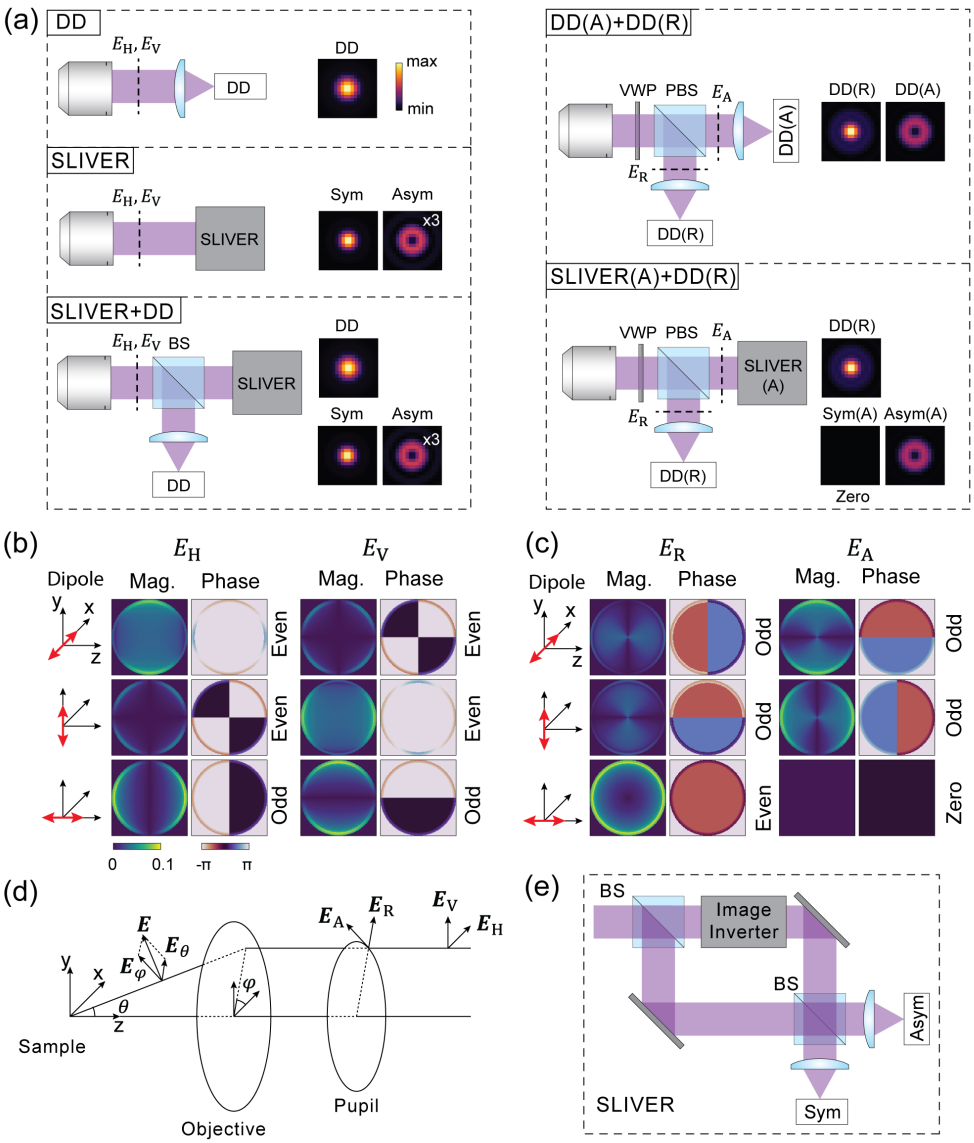

Fig. 1. Illustration of five different detection methods for measuring the separation of two freely rotating dipoles. (a) Schematic drawings of the five detection methods considered in this work and their corresponding PSFs. $\times N$: the image contrast is increased by N times. DD: direct detection, SLIVER: SLIVER detection, H: horizontal, V: vertical, R: radial, A: azimuthal, Sym: symmetric, Asym: antisymmetric, BS: beam splitter, PBS: polarized beam splitter, Mag: magnitude, VWP: vortex wave plate. (b) Pupil magnitudes and phases for horizontal and vertical components of the dipole radiation from dipoles oscillating along x, y and z axes. (c) Pupil magnitudes and phases for the radial and azimuthal components of the dipole radiation from a dipole oscillating along x, y and z axes. (d) Illustration of the coordinate system and definition of the electric fields before and after the objective. See Supplement 1 for detailed derivation of each electric field component. (e) Schematic drawing of the SLIVER detection.

For detection methods with multiple channels, the PSF is a vector of the output intensity distribution from each channel. For freely rotating dipoles, the intensity distributions of the output channels can be obtained as,

$$I_l = \sum_j |\tilde{\omega}_{jl}|^2. \quad j = \mathrm{x, y, z}, \quad l = \mathrm{H, V, R, A}, \tag{7}$$

$$I_{\mathrm{sym},l} = \sum_j \frac{1}{2}|\tilde{\omega}_{jl}(x, y) + \tilde{\omega}_{jl}(-x, -y)|^2, \tag{8}$$

$$I_{\mathrm{asym},l} = \sum_j \frac{1}{2}|\tilde{\omega}_{jl}(x, y) - \tilde{\omega}_{jl}(-x, -y)|^2, \tag{9}$$

where $\tilde{\omega}_{jl}$ is the amplitude PSF of a dipole oriented in j direction and detected with l polarization using DD. The subscript j denotes the dipole oriented in x, y or z direction, while l indicates the electric field at the pupil plane in horizontal (H), vertical (V), radial (R) or azimuthal (A) polarization. In this study, we assume that there are no systematic aberrations from the imaging system, such as coma and astigmatism aberrations induced by optical components. The effect of systematic aberrations on SLIVER detection has been extensively compared in Ref. [40]. Supplement 1 provides detailed derivations of the PSF model for each detection method.

2.3. CRLB calculation

The model of two emitters can be calculated from,

$$I_{2\mathrm{em}} = s \cdot \frac{1}{2} I_1 \left(x - x_0 + \frac{\Delta x}{2}, y - y_0 + \frac{\Delta y}{2} \right) + s \cdot \frac{1}{2} I_2 \left(x - x_0 - \frac{\Delta x}{2}, y - y_0 - \frac{\Delta y}{2} \right) + b, \tag{10}$$

where I_1 and I_2 are PSFs from one of the five detection methods. As two fluorescent molecules of the same type usually have the same emission rate under the same excitation power, we assume $I_1 = I_2$, meaning the two emitters are identical in terms of emission rate and shape. The effect of unequal intensities between two emitters has been well studied in previous works [40, 41]. The displacements $\Delta x = d \cos \alpha$ and $\Delta y = d \sin \alpha$ represent the separation along the x and y axes, with α being the angle between the x-axis and the line defined by two emitters. The estimation parameters include the centroid position (x_0, y_0), the total photon of two emitters s, the separation d, the angle α and the background photon per pixel b. Assuming the photon count from each pixel follows a Poisson distribution and the pixel values are independent of each other, the Fisher information matrix is given by,

$$F_{ij} = \sum_q \frac{1}{I_{2\mathrm{em},q}} \frac{\partial I_{2\mathrm{em},q}}{\partial \theta_i} \frac{\partial I_{2\mathrm{em},q}}{\partial \theta_j}, \quad \theta = (d, \alpha, x_0, y_0, s, b) \tag{11}$$

where q denotes the pixel index. We then compute the CRB for separation estimation from,

$$\sigma_d^2 = (F^{-1})_{11}. \tag{12}$$

If we consider only the estimation of d and assume other parameters are known, the CRB for estimating d is directly given by,

$$\sigma_d^2 = F_{11}^{-1}. \tag{13}$$

It was shown that when d approaches infinity, σ_d^2 approaches the QCRB using a Gaussian PSF model [12]. However, as dipole radiation generates complex and vectorial fields, the calculation of QCRB from a dipole PSF is more complicated. Instead of deriving the QCRB for a dipole PSF, we define a quantity σ_∞ as a reference for quantifying the separation estimation,

$$\sigma_\infty = \lim_{d \to \infty} \sigma_{\mathrm{DD},d}, \tag{14}$$

where $\sigma_{\mathrm{DD},d}$ is the estimation precision of d using DD. We also define

$$\sigma_{\mathrm{psf}} = \frac{1}{2}(\sigma_{\mathrm{DD},x_0} + \sigma_{\mathrm{DD},y_0}), \tag{15}$$

where σ_{DD,x_0} and σ_{DD,y_0} are estimation precisions of the centroid position of a single freely rotating dipole using DD. As the PSF model in DD is circular symmetric, we have $\sigma_{\mathrm{DD},x_0} = \sigma_{\mathrm{DD},y_0}$. We showed that $\sigma_\infty = 2\sigma_{\mathrm{psf}}$ (Supplement 1), which matches the result derived from a Gaussian PSF model [12]. In the following results, unless otherwise specified, we set $s = 1$, $\alpha = 0$, $b = 0$, and $x_0 = y_0 = 0$. Throughout the text, σ_∞ and σ_{psf} are always calculated under the condition of one total photon and zero background.

3. Results

3.1. Precision of separation estimation at different separations

First, we quantified the precision of separation estimation σ_d for different detection methods at various separations d (Fig.2). The two-emitter model $I_{2\mathrm{em}}$ for each detection method was generated by simulating a image of 150×150 pixels for each channel. The image size was chosen large enough so that the σ_{psf} converges. We chose a small pixel size defined by $\lambda/8n_a$, with λ the emission wavelength and n_a the numerical aperture (NA) of the objective lens. The pixel size is set to a value much smaller than the Nyquist sampling to ensure that all features of the PSF patterns are captured. Additionally, even with a small pixel size, the pixel integration needs to be considered. We computed each pixel value as the integral over 2×2 up-sampling points within the pixel. Results in Fig.2 were obtained using a wavelength of $\lambda = 680$ nm and a NA of $n_a = 1.45$, which are typical parameters for oil immersion objectives used in super-resolution imaging of far-red fluorophores. We also incorporated refractive index mismatch (IMM) in the PSF model by setting the refractive indices of the sample medium, coverslip and immersion oil to 1.33, 1.516 and 1.516, respectively. The corresponding pupil functions are shown in Fig.1(b,c), where the bright rings originate from the supercritical angle fluorescence (SAF) caused by IMM [42–44].

We found that the precision of separation estimation is comparable across DD, SLIVER and SLIVER+DD methods at all separations (Fig.2(b)). SLIVER detection is slightly better than SLIVER+DD, suggesting that SLIVER detection alone is sufficient for estimating separations. However, this method is not practical as it requires prior knowledge of the centroid of two emitters. Furthermore, for measuring the separation of two freely rotating dipoles with a high-NA objective, SLIVER offers little advantage over DD. This finding contradicts the previous conclusion drawn from a scalar PSF model, such as a Gaussian PSF model [12]. The PSF of a dipole emitter is described by vectorial diffraction theory, where its PSF cannot be simply calculated from the Fourier transform of a scalar pupil function, but rather an incoherent sum of the contributions from all polarized fields (Supplement 1). In SLIVER detection, the radiation from a freely rotating dipole can be decomposed into six polarized fields: three in horizontal polarization (E_{H}) and three in vertical polarization (E_{V}), corresponding to dipoles oscillating along x, y and z directions (Fig.1(b)). The incoherent sum of those six polarized field mixes even and odd fields, preventing both the symmetric and antisymmetric channels in SLIVER from achieving total constructive or destructive interference. This results in a visibility of less than one, which is detrimental to separation estimation at $d \ll \sigma_{\mathrm{psf}}$. Even a 0.1% decrease in visibility will lead to a rapid divergence in σ_d at small separations (Fig.3). To recover the precision in the presence of freely rotating dipoles, we introduce a VWP after the objective and replace the BS with a PBS. This design decouples the radially (E_{R}) and azimuthally (E_{A}) polarized fields from dipole radiation. Each polarization (R and A) has three fields from three orthogonally orientated dipoles (Fig.1(c)). We identified that azimuthally polarized fields exhibit purely odd symmetry, which is optimal for SLIVER detection. This configuration SLIVER(A) allows for total constructive interference, thereby achieving a visibility of one. Fig.2(b) shows that SLIVER(A)+DD(R)

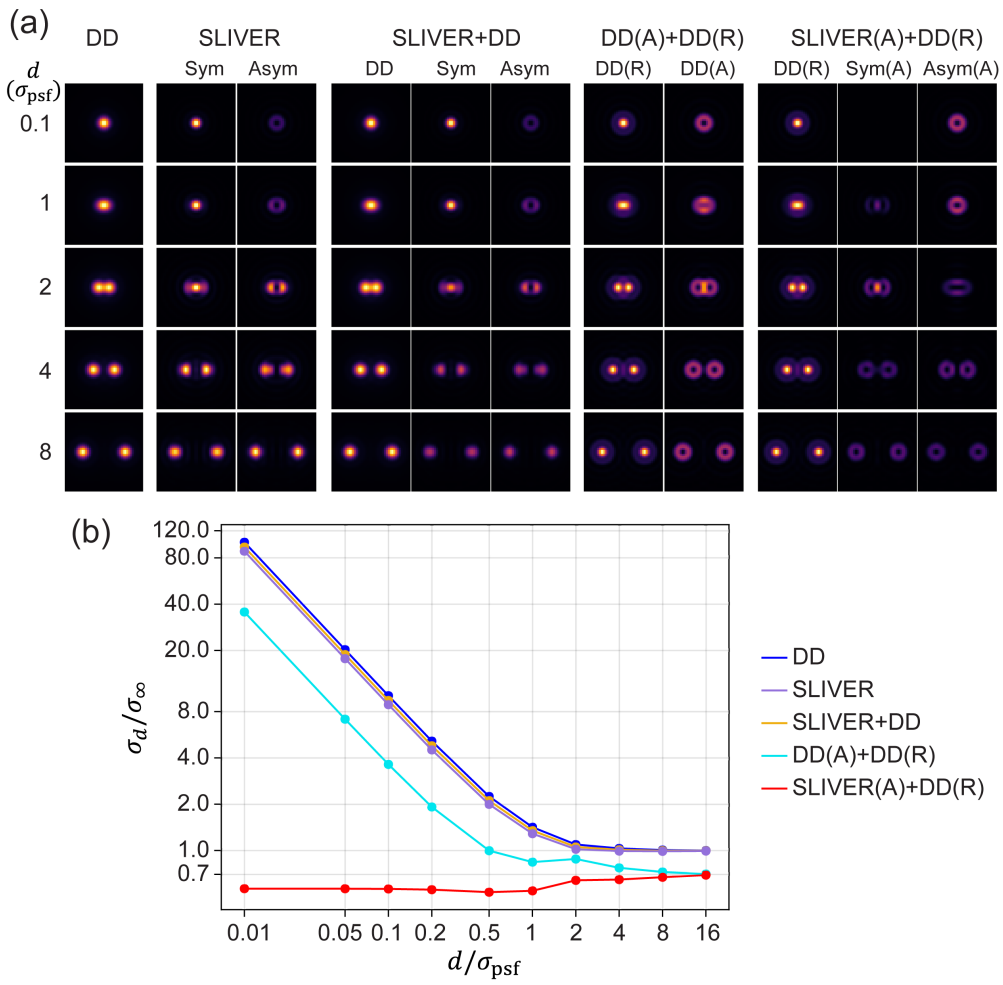

Fig. 2. Comparison of separation estimation precision for various detection methods. (a) Two emitter models of different detection methods at various separations. The intensity is scaled from minimum to maximum values within each detection conditions. (b) Separation estimation precision σ_d under different detection methods. σ_∞ and σ_{psf} are defined in main text.

recovers the precision of separation estimation and achieves $\sigma_d < \sigma_\infty$ at all separations. We noticed that σ_d as $d \to 0$ is even smaller than the values as $d \to \infty$. We showed that this is caused by dipole radiation, where the PSF is the incoherent sum of fields from multiple dipole orientations (Fig. S1 and Supplement 1). To investigate the effect by simply decoupling E_{R} and E_{A}, we calculated σ_d under direct detection of E_{R} and E_{A}, DD(A)+DD(R). We found that although σ_d of DD(A)+DD(R) still diverge as $d \to 0$, the divergence is more than two times smaller than that of DD. This is because the sharper features of the PSFs produced by radially and azimuthally polarized fields (Fig.2(a)) contain more information for separation estimation. Furthermore, as $d \to \infty$, σ_d of DD(A)+DD(R) and SLIVER(A)+DD(R) converge to the same value. This is because their Fisher information for estimating d is equal at $d \to \infty$ (Supplement 1).

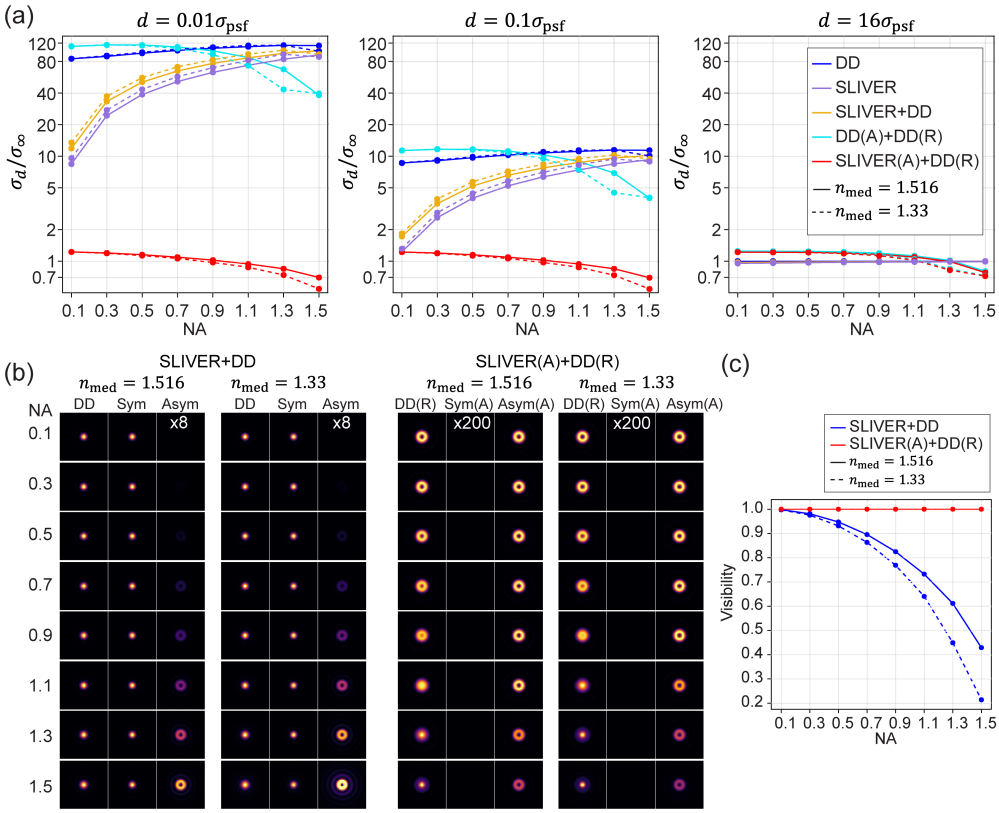

Fig. 3. Effect of numerical aperture on separation estimation precision. (a) Comparison of σ_d versus numerical aperture for different detection methods. Results at separations of $0.01\sigma_{psf}$, $0.1\sigma_{psf}$ and $16\sigma_{psf}$ are shown. For each condition, results with and without index mismatch aberration are compared. Simulation parameters are: $\lambda = 680$ nm, refractive index of sample medium $n_{med} = 1.516$ when index is matched and $n_{med} = 1.33$ when index is mismatched, NA at 0.1 to 1.5 with a step size of 0.2, and the rest parameters are the same as defined in Fig.1. (b) PSFs of different NAs from SLIVER+DD and SLIVER(A)+DD(R). PSFs of index matched ($n_{med} = 1.516$) and index mismatched ($n_{med} = 1.33$) conditions are shown. (c) Comparison of visibilities from SLIVER+DD and SLIVER(A)+DD(R).

3.2. Precision of separation estimation at different numerical apertures

We next investigated the effect of NA on separation estimation (Fig.3(a)). We found that σ_d from the three methods without VWP increases with NA. At low NA (NA<1.1), SLIVER and SLIVER+DD outperforms both DD and DD(A)+DD(R). This is because as NA decreases, the contribution from a dipole oscillating along the z-axis diminishes when most of its radiation is lost at small NAs. Therefore, the radiation collected from a freely rotating dipole predominantly generates even fields, which enhances visibility (Fig. 3(c)) and improves precision. However, even when NA is reduced to 0.1 and the visibility increases to 99.8% (Fig.3(c)), σ_d from SLIVER and SLIVER+DD still diverges as $d \to 0$ (Fig.3(a)), increasing by ~10 times at a separation of $0.01\sigma_{psf}$ compared to at a separation of $16\sigma_{psf}$. At high NA (NA>1.1), both SLIVER and SLIVER+DD perform worse than DD(A)+DD(R) and approach the performance of DD. We also found that IMM ($n_{med} = 1.33$) will further reduce the visibility of SLIVER and SLIVER+DD as NA increases (Fig.3(b,c)). However, this reduction in visibility has a small influence on

separation estimation (Fig.3(a)).

By introducing a VWP in the detection path, the separation estimation favors high NA for both DD(A)+DD(R) and SLIVER(A)+DD(R). As the visibility of SLIVER(A)+DD(R) remains constant and is equal to one at all NAs (Fig.3(c)), σ_d does not diverge as $d \to 0$ (Fig.3(a)). In the case of IMM, σ_d for both DD(A)+DD(R) and SLIVER(A)+DD(R) is further reduced at high NA. However, when NA increases to ~1.4, the Fisher information of estimating d starts to decrease for DD(A)+DD(R) at all separations and for SLIVER(A)+DD(R) as $d \to \infty$ (Fig. S1(b)). This decrease in Fisher information results in corresponding increases in σ_d (Fig. 3(a) and Fig. S1(a)). We also found that as $d \to \infty$, the detection methods with and without VWP converge separately (Fig.3(a)). This difference is because the PSFs without VWP are calculated from horizontally and vertically polarized fields (Fig.1(b)), while the PSFs with VWP are calculated from azimuthally and radially polarized fields (Fig. 1(c)). This results in different Fisher information for estimating d as $d \to \infty$ (Supplement 1).

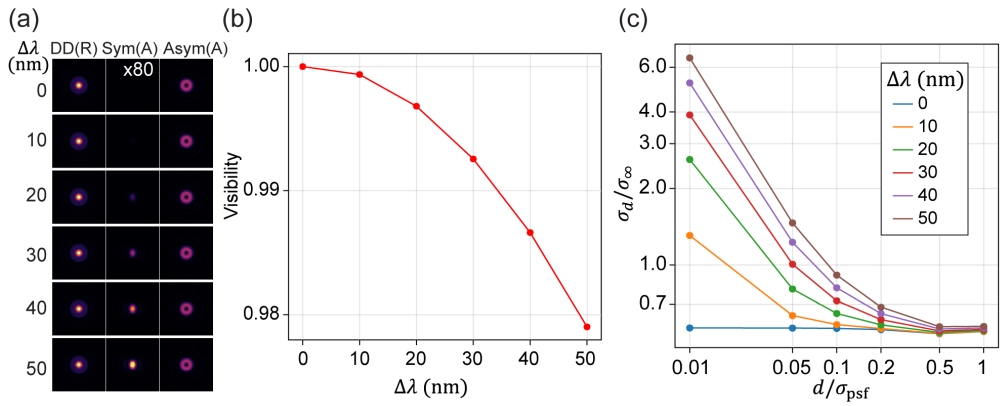

Fig. 4. Effect of detection bandwidth on separation estimation for SLIVER(A)+DD(R). (a) PSFs of SLIVER(A)+DD(R) at various detection bandwidth, $\Delta\lambda$. (b) Visibility versus $\Delta\lambda$. (c) σ_d versus separation at various $\Delta\lambda$. Simulation parameters are: $n_a = 1.45$, $\lambda = 680$ nm, $n_{\text{med}} = 1.33$, the VWP is optimized at 680 nm.

3.3. Practical considerations

3.3.1. Effect of detection bandwidth

The above calculations consider an ideal VWP, which can convert a radially/azimuthally polarized field to horizontally/vertically polarized field at 100% efficiency. However, fluorescence emission often has a broad spectrum. To achieve 100% conversion efficiency, a single VWP has to be optimized for a broad spectral range. To our knowledge, broad-band VWP is more complicated in fabrication and has lower transmission efficiency [45]. Here we consider a commonly used commercial VWP (e.g. WPV10L-633, Thorlabs) that is only optimized for a single wavelength. This VWP is fabricated from nematic liquid crystal (LC), with LC molecules aligned azimuthally to create a half-wave plate with spatially varied fast axis [46]. We simulate the VWP based on the dispersion of nematic LC, where the phase delay between the extraordinary and ordinary polarizations is given by $\delta = 2\pi(n_{\text{e}} - n_{\text{o}})t/\lambda$, with t being the thickness of the VWP and n_e and n_o being the refractive indices of corresponding polarizations. This VWP can only be optimized for a single wavelength that satisfies the half-wave delay condition, $\delta = \pi$, ensuring 100% conversion efficiency. However, the conversion efficiency of the VWP decreases as the detection bandwidth ($\Delta\lambda$), defined by the emission filter, increases. With partial conversion, the

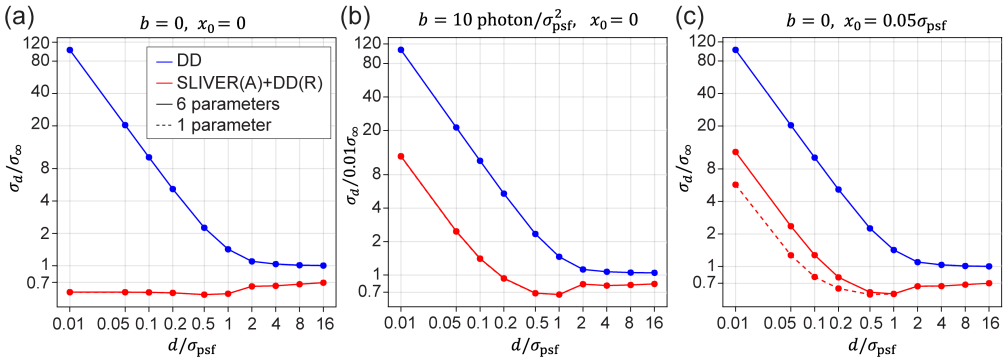

Fig. 5. Effect of number of estimation parameters on separation estimation. Precisions of separation estimation by estimating d only (solid lines) and by estimating all six parameters together (dash lines), using DD or SLIVER(A)+DD(R), are shown. (a) Results under the ideal condition. (b) Results under the condition of non-zero background: $b = 10$ photon$/\sigma_{\rm psf}^2$, total photon $s = 10000$. (c) Results under the condition of misalignment: $x_0 = 0.05\ \sigma_{\rm psf}$. Simulation parameters are: $n_a = 1.45$, $\lambda = 680$ nm, $n_{\rm med} = 1.33$, total photon $s = 1$ for (a) and (c), VWP is ideal.

fields entering the SLIVER detection arm will not be purely azimuthal polarized, preventing total destructive interference in the symmetric channel (Fig.4(a)). Consequently, the visibility reduces with increasing $\Delta\lambda$, leading to a divergence of σ_d as $d \to 0$ (Fig.4(b,c)). Due to the larger dispersion of nematic LCs at shorter wavelengths, the visibility decreases faster as $\Delta\lambda$ increases, resulting in a larger divergence of σ_d at shorter wavelengths (Fig. S2). For super-resolution imaging, the emission filter typically has a bandwidth of 30-50 nm to achieve a high signal-to-noise ratio. Within this bandwidth range, the divergence is relatively small compared to the other four methods (Fig.2(b)).

3.3.2. Effect of number of estimation parameters

The above results were obtained by considering the separation d as the only estimation parameter, assuming other parameters are known. We next examine the estimation precision of d when estimating all parameters together (full-parameter estimation). The parameters were defined in Eq. (10). Here we focus on the SLIVER(A)+DD(R) and DD methods. We found that σ_d has negligible variations between full-parameter (six parameters) and one-parameter estimations for both detection methods under the ideal condition (Fig. 5(a)). We next investigate the impact of the number of estimation parameters when introducing a non-zero background photon per pixel or a slight misalignment of the centroid positions of two emitters (refer to sections 3.3.3 and 3.3.4 for further discussion on background and misalignment). We found that under the condition of a non-zero background, the number of estimation parameters also has little effect on σ_d for both SLIVER(A)+DD(R) and DD (Fig. 5(b)). However, for SLIVER(A)+DD(R), when the centroid of two emitters is misaligned with the inversion center of SLIVER(A), σ_d is smaller when estimating d only (Fig. 5(c)). For DD, since the separation estimation is independent of the centroid position, an offset of the centroid position does not affect the estimation of d in both one-parameter and full-parameter estimations. Furthermore, as the PSF in SLIVER(A)+DD(R) is circular symmetric, the angle α has little effect on the separation estimation in full-parameter estimation (Fig. S3(b,c)), and σ_d is the same as the one from one-parameter estimation (Fig. 2(b)) . We noticed that the angle estimation precision σ_α diverges quickly as $d \to 0$, which implies that SLIVER(A)+DD(R) is not optimal for angle estimation (Fig. S3(d,e)). However, compared to DD, SLIVER(A)+DD(R) still performs better in angle estimation (Fig.S4(b) and

Fig.S5(b)).

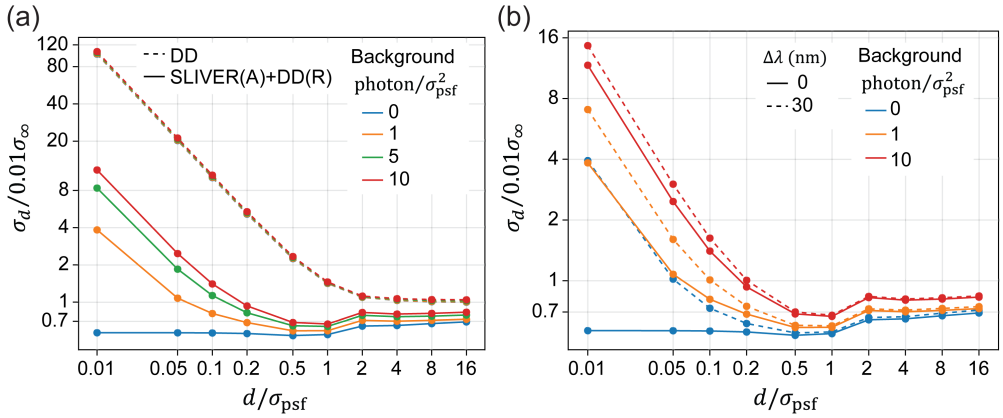

Fig. 6. Effect of background on separation estimation. (a) Comparison of separation estimation of DD and SLIVER(A)+DD(R) at different background levels. Simulation parameters are: $n_a = 1.45$, $\lambda = 680$ nm, $n_{\text{med}} = 1.33$, total photon $s = 10000$, VWP is ideal. (b) Separation estimation precision of SLIVER(A)+DD(R) at different background levels and detection bandwidths. Simulation parameters are: $n_a = 1.45$, $\lambda = 680$ nm, $n_{\text{med}} = 1.33$, total photon $s = 10000$, VWP is optimized at 680 nm. Precisions were calculated under full parameter estimation.

3.3.3. Effect of background on separation estimation

In fluorescence imaging, background is often inevitable. Background mainly comes from out-of-focus fluorophores, sample autofluorescence and impurities of the coverslip surface. Here we investigate the impact of non-zero background on separation estimation. We simulated data with 10,000 total photons per measurement and added a constant background photon per pixel. We define a background unit as photon per σ_{psf}^2, which can be interpreted as photon per pixel when the pixel size is σ_{psf}. We found that for SLIVER(A)+DD(R), even with a background level of 1 photon/σ_{psf}^2, the precision of separation estimation starts to diverge (Fig. 6(a)) as $d \to 0$. This divergence continuously increases with increasing background. However, within a common background range (1-10 photon/σ_{psf}^2) at low labeling density, SLIVER(A)+DD(R) still outperforms DD by a factor of 6 as $d \to 0$. We noticed that background has minimal impact on separation estimation using DD. This is also true for angle and centroid estimation, where background has less effect on DD (Fig. S4(b-d)). For estimations of total photons and background photons, the background has similar effect on both DD and SLIVER(A)+DD(R) (Fig. S4(e,f)). Additionally, adding a detection bandwidth of 30 nm further increases σ_d, however, the increase is less at higher background levels (Fig.6(b)).

3.3.4. Effect of misalignment on separation estimation

Lastly, we examine the effect of misalignment between the centroid of two emitters and the inversion center of the SLIVER(A) detection. For SLIVER(A)+DD(R), the Fisher information for separation estimation drops to zero as $d \to 0$ with even a small misalignment of the centroid position. We introduce a misalignment by adding an offset to the centroid position along the x-axis (x_0). Fig. 7(a) shows that at a misalignment of 0.01 to $0.1\sigma_{\text{psf}}$, the precision of separation estimation increases by 3.5 to 35 times at a separation of $0.01\sigma_{\text{psf}}$. However, for DD, as there is no image inversion, the centroid position has no impact on the separation estimation (Fig. 7(a)). This is also true for estimating other parameters using DD (Fig. S5(b-f)). For

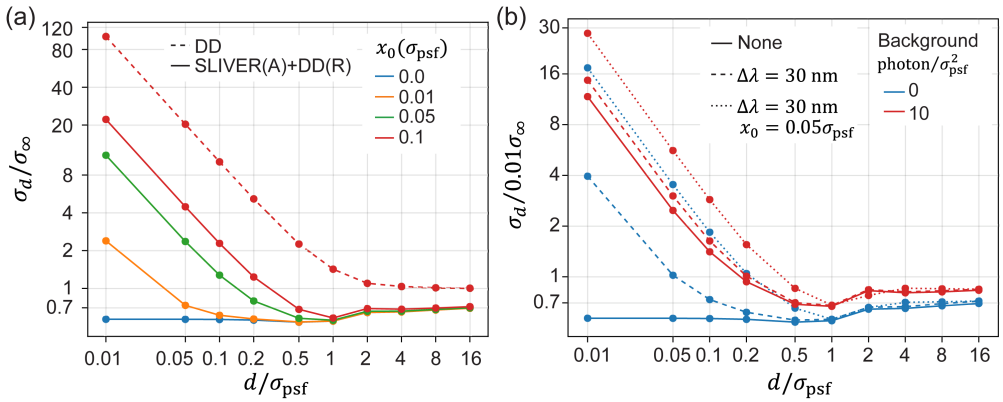

Fig. 7. Effect of misalignment on separation estimation. (a) Comparison of separation estimation of DD and SLIVER(A)+DD(R) at different amounts of misalignment. Misalignment is introduced by adding an offset to the centroid position along the x-axis (x_0). Simulation parameters are: $n_a = 1.45$, $\lambda = 680$ nm, $n_{\text{med}} = 1.33$, total photon $s = 1$, background $b = 0$, VWP is ideal. (b) Separation estimation precision of SLIVER(A)+DD(R) at different background levels, under the conditions of zero detection bandwidth and zero misalignment (solid line), a detection bandwidth of 30 nm and zero misalignment (dash line), and a detection bandwidth of 30 nm plus a misalignment of $0.05\sigma_{\text{psf}}$ (dotted line). Simulation parameters are: $n_a = 1.45$, $n_{\text{med}} = 1.33$, total photon $s = 10000$, VWP is optimized at 680 nm. Precisions were calculated under full parameter estimation.

SLIVER(A)+DD(R), misalignment will also increase the precision of angle estimation, but slightly decrease the precision of centroid estimation (Fig. S5(b-d)). Next, we study the condition when combining the effects of detection bandwidth, background and misalignment. We find that with a detection bandwidth of 30 nm, the addition of a misalignment of $0.05\sigma_{\text{psf}}$ further increases the precision of separation estimation by 2-4 folds under different background levels. This indicates that misalignment has a more dominant effect on separation estimation compared to detection bandwidth and background. In practice, the precision of centroid estimation is around $\sigma_{\text{psf}}/\sqrt{s}$, where s is the total photon count of two emitters. To achieve a misalignment within $0.05\sigma_{\text{psf}}$, a total photon count of $s > 2000$ is required.

4. Discussion and Conclusion

In this study, we introduce a novel detection method, SLIVER(A)+DD(R), which has the potential to optimally measure the separation of two freely rotating dipoles. We evaluated separation estimation using five different detection methods and demonstrated that SLIVER(A)+DD(R) outperforms the others. Under the ideal condition, SLIVER(A)+DD(R) maintains nearly constant precision in separation estimation across all separations. We also examined the impact of numerical aperture, detection bandwidth, the number of estimation parameters, background, and misalignment on separation estimation. Our findings indicate that, even with these practical considerations, SLIVER(A)+DD(R) continues to outperform the other methods.

To experimentally realize SLIVER(A)+DD(R), several aspects should be considered. First, SLIVER(A)+DD(R) relies on a device that can convert radial/azimuthal polarization to horizontal/vertical polarization. This conversion falls into the category of spin-angular-momentum (SAM) to orbital-angular-momentum (OAM) conversion of light [47, 48]. Many techniques have been developed to achieve SAM-OAM conversion. Future development will include exploring the optimal SAM-OAM conversion method for the experimental implementation

of SLIVER(A)+DD(R). Furthermore, SLIVER(A) requires the centroid of two emitters to be aligned with the inversion center, which limits the measurement to one dimer molecule at a time. To achieve high-throughput imaging, SLIVER(A)+DD(R) can be combined with high-speed single particle tracking for fast repositioning of the centroid. Lastly, to exploit the full potential of SLIVER(A)+DD(R), techniques that minimize background fluorescence are also critical for actual implementation.

We anticipate that SLIVER(A)+DD(R) will enable distance measurement of dipole emitters to approach the QCRB limited precision and will find broad applications in fluorescence microscopy, where many fluorescence molecules are modeled as dipole emitters.

Acknowledgment. This work was conducted with the supports from National Institutes of Health grant 1R01GM140284 and University of New Mexico Office of the Vice President for Research Program for Enhancing Research Capacity.

Disclosures. The authors declare no conflicts of interest.

Supplemental document. See Supplement 1 for supporting content.

References

1. Rayleigh, "XXXI. *Investigations in optics, with special reference to the spectroscope*," The London, Edinburgh, Dublin Philos. Mag. J. Sci. **8**, 261–274 (1879).
2. J. W. Goodman, *Introduction to Fourier optics, Third Edition* (Roberts and Company Publishers, 2005), 3rd ed.
3. S. M. Kay, *Fundamentals of Statistical Signal Processing: Estimation Theory* (Prentice Hall, 1993).
4. C. R. Rao, *Linear Statistical Inference and its Applications: Second Editon*, Wiley Series in Probability and Statistics (Wiley, 1973), 1st ed.
5. R. J. Ober, S. Ram, and E. S. Ward, "Localization Accuracy in Single-Molecule Microscopy," Biophys. J. **86**, 1185–1200 (2004).
6. C. V. Middendorff, A. Egner, C. Geisler, *et al.*, "Isotropic 3D Nanoscopy based on single emitter switching," Opt. Express **16**, 20774 (2008).
7. C. S. Smith, N. Joseph, B. Rieger, and K. A. Lidke, "Fast, single-molecule localization that achieves theoretically minimum uncertainty," Nat. Methods **7**, 373–375 (2010).
8. Y. Shechtman, S. J. Sahl, A. S. Backer, and W. Moerner, "Optimal Point Spread Function Design for 3D Imaging," Phys. Rev. Lett. **113**, 133902 (2014).
9. S. Liu and F. Huang, "Enhanced 4Pi single-molecule localization microscopy with coherent pupil based localization," Commun. Biol. **3**, 220 (2020).
10. Y. Li, W. Shi, S. Liu, *et al.*, "Global fitting for high-accuracy multi-channel single-molecule localization," Nat. Commun. **13**, 3133 (2022).
11. P. Zhang, S. Liu, A. Chaurasia, *et al.*, "Analyzing complex single-molecule emission patterns with deep learning," Nat. Methods **15**, 913–916 (2018).
12. M. Tsang, R. Nair, and X.-M. Lu, "Quantum Theory of Superresolution for Two Incoherent Optical Point Sources," Phys. Rev. X **6**, 031033 (2016).
13. F. Huang, S. L. Schwartz, J. M. Byars, and K. A. Lidke, "Simultaneous multiple-emitter fitting for single molecule super-resolution imaging," Biomed. Opt. Express **2**, 1377 (2011).
14. C. W. Helstrom, "Quantum detection and estimation theory," J. Stat. Phys. **1**, 231–252 (1969).
15. S. L. Braunstein and C. M. Caves, "Statistical distance and the geometry of quantum states," Phys. Rev. Lett. **72**, 3439–3443 (1994).
16. M. P. Backlund, Y. Shechtman, and R. L. Walsworth, "Fundamental Precision Bounds for Three-Dimensional Optical Localization Microscopy with Poisson Statistics," Phys. Rev. Lett. **121**, 023904 (2018).
17. O. Zhang and M. D. Lew, "Quantum limits for precisely estimating the orientation and wobble of dipole emitters," Phys. Rev. Res. **2**, 033114 (2020).
18. V. Giovannetti, S. Lloyd, and L. Maccone, "Advances in quantum metrology," Nat. Photonics **5**, 222–229 (2011).
19. G. TÃşth and I. Apellaniz, "Quantum metrology from a quantum information science perspective," J. Phys. A: Math. Theor. **47**, 424006 (2014).
20. M. Tsang, "Subdiffraction incoherent optical imaging via spatial-mode demultiplexing," New J. Phys. **19**, 023054 (2017).
21. M. Tsang, "Subdiffraction incoherent optical imaging via spatial-mode demultiplexing: Semiclassical treatment," Phys. Rev. A **97**, 023830 (2018).
22. N. K. Fontaine, R. Ryf, H. Chen, *et al.*, "Laguerre-Gaussian mode sorter," Nat. Commun. **10**, 1865 (2019).
23. P. Boucher, C. Fabre, G. Labroille, and N. Treps, "Spatial optical mode demultiplexing as a practical tool for optimal transverse distance estimation," Optica **7**, 1621 (2020).
24. F. Yang, A. Tashchilina, E. S. Moiseev, *et al.*, "Far-field linear optical superresolution via heterodyne detection in a higher-order local oscillator mode," Optica **3**, 1148 (2016).

25. A. Pushkina, G. Maltese, J. Costa-Filho, *et al.*, “Superresolution Linear Optical Imaging in the Far Field,” Phys. Rev. Lett. **127**, 253602 (2021).
26. A. Duplinskiy, J. Frank, K. Bearne, and A. I. Lvovsky, “Tsang’s resolution enhancement method for imaging with focused illumination,” (2024). ArXiv:2405.20979 [physics, physics:quant-ph].
27. M. Paur, B. Stoklasa, Z. Hradil, *et al.*, “Achieving quantum-limited optical resolution,” (2016). Version Number: 1.
28. W.-K. Tham, H. Ferretti, and A. M. Steinberg, “Beating RayleighâĂŹs Curse by Imaging Using Phase Information,” Phys. Rev. Lett. **118**, 070801 (2017).
29. R. Nair and M. Tsang, “Interferometric superlocalization of two incoherent optical point sources,” Opt. Express **24**, 3684 (2016).
30. Z. S. Tang, K. Durak, and A. Ling, “Fault-tolerant and finite-error localization for point emitters within the diffraction limit,” Opt. Express **24**, 22004 (2016).
31. M. BÃűhmer and J. Enderlein, “Orientation imaging of single molecules by wide-field epifluorescence microscopy,” J. Opt. Soc. Am. B **20**, 554 (2003).
32. J. Enderlein, E. Toprak, and P. R. Selvin, “Polarization effect on position accuracy of fluorophore localization,” Opt. Express **14**, 8111 (2006).
33. S. Stallinga and B. Rieger, “Accuracy of the Gaussian Point Spread Function model in 2D localization microscopy,” Opt. Express **18**, 24461 (2010).
34. K. I. Mortensen, L. S. Churchman, J. A. Spudich, and H. Flyvbjerg, “Optimized localization analysis for single-molecule tracking and super-resolution microscopy,” Nat. Methods **7**, 377–381 (2010).
35. M. P. Backlund, M. D. Lew, A. S. Backer, *et al.*, “The Role of Molecular Dipole Orientation in Single-Molecule Fluorescence Microscopy and Implications for Super-Resolution Imaging,” ChemPhysChem **15**, 587–599 (2014).
36. K. I. Mortensen, J. Sung, H. Flyvbjerg, and J. A. Spudich, “Optimized measurements of separations and angles between intra-molecular fluorescent markers,” Nat. Commun. **6**, 8621 (2015).
37. C. N. Hulleman, R. Ã. Thorsen, E. Kim, *et al.*, “Simultaneous orientation and 3D localization microscopy with a Vortex point spread function,” Nat. Commun. **12**, 5934 (2021).
38. T. Wu, J. Lu, and M. D. Lew, “pixOL: pixel-wise dipole-spread function engineering for simultaneously measuring the 3D orientation and 3D localization of dipole-like emitters,” preprint, Molecular Biology (2021).
39. S. Liu, J. Chen, J. Hellgoth, *et al.*, “Universal inverse modeling of point spread functions for SMLM localization and microscope characterization,” Nat. Methods **21**, 1082–1093 (2024).
40. D. J. Schodt, P. J. Cutler, F. E. Becerra, and K. A. Lidke, “Tolerance to aberration and misalignment in a two-point-resolving image inversion interferometer,” Opt. Express **31**, 16393 (2023).
41. J. ÅŸehaÄĢek, Z. Hradil, B. Stoklasa, *et al.*, “Multiparameter quantum metrology of incoherent point sources: Towards realistic superresolution,” Phys. Rev. A **96**, 062107 (2017).
42. D. Axelrod, “Fluorescence excitation and imaging of single molecules near dielectric-coated and bare surfaces: a theoretical study,” J. Microsc. **247**, 147–160 (2012).
43. A. Dasgupta, J. Deschamps, U. Matti, *et al.*, “Direct supercritical angle localization microscopy for nanometer 3D superresolution,” Nat. Commun. **12**, 1180 (2021).
44. S. Liu, E. B. Kromann, W. D. Krueger, *et al.*, “Three dimensional single molecule localization using a phase retrieved pupil function,” Opt. Express **21**, 29462 (2013).
45. M. P. Backlund, A. Arbabi, P. N. Petrov, *et al.*, “Removing orientation-induced localization biases in single-molecule microscopy using a broadband metasurface mask,” Nat. Photonics **10**, 459–462 (2016).
46. A. Rubano, F. Cardano, B. Piccirillo, and L. Marrucci, “Q-plate technology: a progress review [Invited],” J. Opt. Soc. Am. B **36**, D70 (2019).
47. Y. Shen, X. Wang, Z. Xie, *et al.*, “Optical vortices 30 years on: OAM manipulation from topological charge to multiple singularities,” Light. Sci. & Appl. **8**, 90 (2019).
48. R. C. Devlin, A. Ambrosio, N. A. Rubin, *et al.*, “Arbitrary spin-toâĂŞorbital angular momentum conversion of light,” Science **358**, 896–901 (2017).